Journal of
Materials Chemistry A

ROYAL SOCIETY
OF CHEMISTRY

PAPER

View Article Online
View Journal

Check for updates

Cite this: DOI: 10.1039/d5ta10322c

Janus NiN_4–CuN_4 catalyst supported by a double-layered ZIF-8 structure for CO_2 electrocatalytic reduction to C_{2+} products

Gege Zhang, Qianyun Tan, Xiaoyu Xu and Fa-Qian Liu *

Received 18th December 2025
Accepted 20th February 2026

DOI: 10.1039/d5ta10322c

rsc.li/materials-a

Copper (Cu)-based catalysts exhibit considerable potential for the electrocatalytic CO_2 reduction reaction (CO_2RR) to multi-carbon (C_{2+}) products; nevertheless, competitive products (*e.g.*, formic acid) have also been produced by thermodynamic constraints. The attainment of selective C_{2+} products exhibiting high faradaic efficiency (FE) and current density remains a significant challenge. Here, we designed a tandem catalytic strategy and prepared a series of Janus catalysts supported by double-layered ZIF-8 with inner MN_4 and outer CuN_4 for C_{2+} products (especially *n*-propanol). The synthetic catalyst, $NiN_4@CuN_4$, achieved high faradaic efficiencies of 80.6% for C_{2+} at −1.6 V in a flow cell, with 24.4% *n*-propanol ($CH_3CH_2CH_2OH$) and 36.6% ethanol (CH_3CH_2OH). *In situ* Raman experiments along with mechanism analysis indicate that the synergistic interaction of inner NiN_4 and outer CuN_4 significantly facilitates CO production and CO electroreduction, thereby greatly promoting C_{2+} production.

1 Introduction

The transformation of CO_2 into valuable fuels and the utilization of renewable energy resources are prospective avenues for achieving carbon neutrality.[1–6] It is a well-established fact that C_{2+} products, exemplified by C_2H_4, C_3H_7OH and C_2H_5OH, exhibit superior energy density and economic value in comparison to their C_1 counterparts. The following compounds are included in this category: methane (CH_4), formic acid (HCOOH) and carbon monoxide (CO).[7] The complex pathways of electron and proton transfer that occur in the CO_2RR give rise to the emergence of competing reactions, such as the generation of C_1 products and the hydrogen evolution reaction (HER).[8] These competing reactions act as a thermodynamic limitation on the formative process of C_{2+} products. Additionally, the inherent slowness of the C–C coupling process represents a kinetic limitation on the C_{2+} production.[9,10] The extant literature has demonstrated the considerable potential of Cu-based catalysts for the production of C_{2+}.[11] Significant endeavors have been undertaken to attain elevated CO_2RR selectivity and activity. Strategies such as tandem catalysis[12–14] and single atom[15–17] active sites have been extensively studied, but $FE_{C_{2+}}$ is still below that of the C_1 products (FE_{C_1}).

Single-atom catalysts are defined as catalysts in which high atom utilization is achieved through the dispersion of metal atoms.[18] For instance, Gu *et al.*[19] published an innovative N-triggered Zn single-atom catalyst that exhibited excellent oxygen reduction reaction (ORR) performance and low overpotential. Presently, single-atom catalysts are being researched for the CO_2RR, with most studies focusing on CO. Single-atom transition metal catalysts, including Fe,[20–22] Co,[23–25] and Ni,[26–28] primarily facilitate the electroreduction of CO_2 to C_1 products through electrocatalysis. Furthermore, C–C coupling can only be achieved effectively by Cu-based catalysts. Nevertheless, the restricted number of catalytic sites and the considerable distance between them render the conversion of C_2 products with a single Cu single-atom catalyst an arduous task.

Janus catalysts have the capacity to separate two metals, and they are frequently employed catalysts in tandem catalysis.[29] Nanoparticles exhibiting high activity in cascade catalytic reactions are produced by Janus catalysts with multifunctional active sites that possess diverse catalytic properties. Transition metal monoatomic materials (*e.g.*, Fe, Co, Ni) generate high concentrations of CO during CO_2 electroreduction; this CO then promotes C_2 product formation over Cu-based catalysts. Zhang *et al.*[30] reported that a gas diffusion electrode achieved high CO utilization efficiency and high $FE_{C_{2+}}$ through two segments catalyzed in series. Janus catalysts represent a strategy of considerable merit for efficient CO_2 tandem catalysis. Nevertheless, this material is currently the subject of less study compared to other areas, and its synthesis is extremely challenging.

Herein, in this study, we prepared a series of $MN_4@CuN_4$ catalysts with a two-layer ZIF-8 structure, which was capable of enriching CO and achieving high efficiency in the tandem catalysis of carbon dioxide. The synthetic catalyst, $NiN_4@CuN_4$, achieved 81.0% FE_{C2+} at −1.6 V *vs.* RHE potential in 1 M KOH, with 24.4% $CH_3CH_2CH_2OH$ and 36.6% CH_3CH_2OH. This work employs a range of transition metals (including Fe, Co, and Ni) as the CO_2 activation site, utilizes the double-layered structure

---

School of Chemical Engineering and Technology, Sun Yat-sen University, Zhuhai 519082, China. E-mail: liufq7@mail.sysu.edu.cn

to facilitate CO enrichment, and offers a high CO concentration at the outer CuN_4 site. This provides a new strategy of electrocatalyst synthesis for transformation of the CO_2RR into a C_{2+} generation reaction.

2 Experimental section

2.1 Reagents and materials

Zinc acetate dihydrate ($Zn(CH_3COO)_2 \cdot 2H_2O$), nickel(II) chloride hexahydrate ($NiCl_2 \cdot 6H_2O$), iron(II) sulfate heptahydrate ($FeSO_4 \cdot 7H_2O$), 2-methylimidazole (2-MeIm), cobalt(II) chloride hexahydrate ($CoCl_2 \cdot 6H_2O$), copper(II) chloride dihydrate ($CuCl_2 \cdot 2H_2O$), 1,10-phenanthroline, Nafion 117 solution, and potassium hydroxide (KOH) were analytical grade and purchased from Shanghai Macklin Biochemical Technology Company. Methanol (MeOH), (methyl sulfoxide)-d_6 (DMSO-d_6), deuterium oxide (D_2O) and anhydrous ethanol (EtOH) were purchased from Shanghai Aladdin Biochemical Technology Co. Ltd. High purity CO_2 (99.999%) and N_2 (99.999%) were purchased from Zhuhai Huaxin Gas Co. Ltd. All the chemicals and reagents were used without further purification.

2.2 Synthesis of Niphen@ZIF-8

A solution of 0.357 g $NiCl_2 \cdot 6H_2O$ and 0.743 g 1,10-phenanthroline in 120 mL methanol was prepared and stirred for 0.5 h. Subsequently, 4.61 g $Zn(CH_3COO)_2 \cdot 2H_2O$ was added to the solution and stirred for 1 h. The aforementioned solution was then added dropwise to a solution of 17.2 g 2-MeIm in 10 mL of methanol, which was stirred for 5 min and allowed to precipitate for 24 h. The products were washed with methanol, centrifuged three times and then dried in a vacuum at 60 °C. The product was prepared and named Niphen@ZIF-8.

2.3 Synthesis of Niphen@ZIF-8@Cuphen

Niphen@ZIF-8 was added into 120 mL of methanol and dispersed into a 3 mg mL^{-1} suspension. 0.341 g $CuCl_2 \cdot 2H_2O$ was added and stirred for 0.5 h. Subsequently, 0.991 g 1,10-phenanthroline was added and stirred for 1 h. The products were washed with methanol, centrifuged three times and then dried in a vacuum at 60 °C. Finally, Niphen@ZIF-8@Cuphen was obtained.

2.4 Synthesis of Niphen@ZIF-8@Cuphen@ZIF-8

Niphen@ZIF-8@Cuphen was added into 40 mL of methanol and dispersed into a 3 mg mL^{-1} suspension. 1.76 g $Zn(CH_3COO)_2 \cdot 2H_2O$ was added and stirred for 1 h. Subsequently, 0.991 g 1,10-phenanthroline was added and stirred for 24 h. The product was washed with methanol, centrifuged three times and then dried in a vacuum at 60 °C. The final product was labelled Niphen@ZIF-8@Cuphen@ZIF-8.

2.5 Synthesis of NiN_4@CuN_4

250 mg Niphen@ZIF-8@Cuphen@ZIF-8 was heated to 900 °C under N_2 in a tube furnace at 5 °C min^{-1} and held for 2 h. After cooling, black NiN_4@CuN_4, was collected.

2.6 Synthesis of CoN_4@CuN_4 and FeN_4@CuN_4

CoN4@CuN4 and FeN4@CuN4 were obtained by replacing 0.357 g $NiCl_2 \cdot 6H_2O$ with 0.357 g $CoCl_2 \cdot 6H_2O$ and 0.357 g $FeSO_4 \cdot 7H_2O$, and other steps were the same as in the preparation of NiN_4@CuN_4.

2.7 Electrochemical measurements

Electrochemical tests were undertaken within an airtight flow cell, using a Chenhua 660e electrochemical workstation. The carbon paper working electrode was loaded with the catalyst at a density of 1 mg cm^{-2} and measured. The counter electrode and reference electrode were a 1 cm^2 platinum sheet and a Hg/HgO electrode, respectively. Cathode and anode compartments in the flow cell were divided by an anion-exchange membrane (AEM). Both compartments contained 1 M aqueous KOH electrolyte, with flow rates controlled by a peristaltic pump at 10 mL min^{-1}. Flow rates of carbon dioxide (CO_2) were regulated by a digital gas flow controller, set at 20 standard cubic centimeters per minute (sccm). It is important to note that not all measured voltages were *IR*-compensated; however, they were all subjected to conversion to the reversible hydrogen electrode (RHE) potential. The conversion formula is E (*vs.* RHE) = E (*vs.* Hg/HgO) + 0.095 V + 0.0591 V × pH.

2.8 Quantitative analysis of gas and liquid products

The gaseous products were subjected to analysis by gas chromatography equipped with FID and TCD detectors. The FE of gaseous products was calculated as follows:w

$$\mathrm{FE}(\%) = \frac{z \times n \times F}{Q} \times 100\% = \frac{xvzPF}{IRT} \times 100\%$$

here z represents the number of exchanged electrons for CO_2 electroreduction to a specific product, n is the molar quantity of a specific electrocatalytic product, F is the faradaic constant (96 485C mol^{-1}), the term "Q" is used to denote the charge quantity passing through the working electrode during the electrocatalytic process, x is the volume concentration of the gaseous product, the term "v" is the flow rate of CO_2, the term "P" is the standard atmospheric pressure, I is the current passing through the working electrode during electrocatalysis, R is the gas parameter (8.314 J mol^{-1} K^{-1}), and the term "T" is the room temperature.

The liquid product was determined by ^1H NMR spectra. 500 μL of the electrolyte after the CO_2RR and 100 μL of D_2O containing 50 ppm (m m^{-1}) dimethyl sulfoxide as an internal standard were used to determine the product-specific Faraday efficiency on a Bruker 400 MHz spectrometer. The Faraday efficiency of the liquid product was calculated as follows:w

$$\mathrm{FE}_{\mathrm{liquid}}\% = \frac{Q_{\mathrm{product}}}{Q_{\mathrm{total}}} \times 100\% = \frac{mFn}{It} \times 100\%$$

here Q_{total} represents the total charge consumed during the electrolysis, Q_{product} is the charge during the formation of the liquid product, m represents the number of exchanged electrons for the CO_2RR, n is the number of moles of a certain product, and the term "t" is electrolysis time.

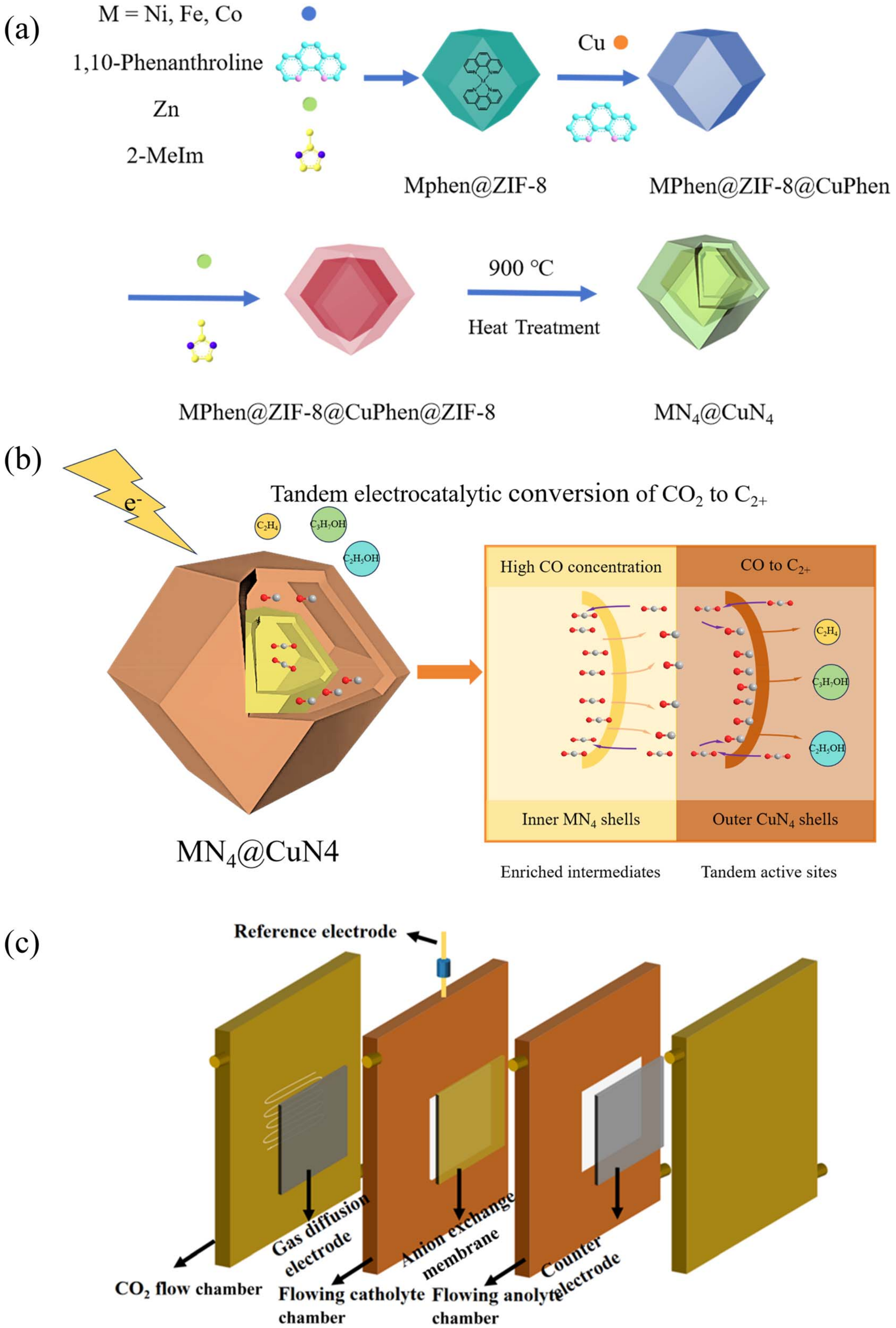

Fig. 1 (a) The synthesis route of Janus catalyst $MN_4@CuN_4$ supported by double-layered ZIF-8, (b) the generation process of C_{2+} products on MN_4CuN_4, and (c) schematic representation of the flow cell.

3 Results and discussion

3.1 Morphological and structural investigation

The tandem catalyst, $NiN_4@CuN_4$, was prepared layer by layer using a bottom–up strategy. The synthesis route is shown in Fig. 1a. Subsequent to a 900 °C treatment, a double-layered carbon material containing an inner NiN_4 site and outer CuN_4 was prepared.[31] The synthesized materials were analyzed *via* XRD, and the resulting pattern is presented in Fig. 2a. The standard XRD pattern of ZIF-8 is shown. It is evident that the structures of Niphen@ZIF-8, Niphen@ZIF-8@Cuphen and Niphen@ZIF-8@Cuphen@ ZIF-8 were consistent with the ZIF-8 standard card, thereby demonstrating the retention of identical structural characteristics. The examination of Ni and Cu was not conducted due to their low content.[32] The X-ray diffraction (XRD) pattern of $NiN_4@CuN_4$, $CoN_4@CuN_4$ and $FeN_4@CuN_4$

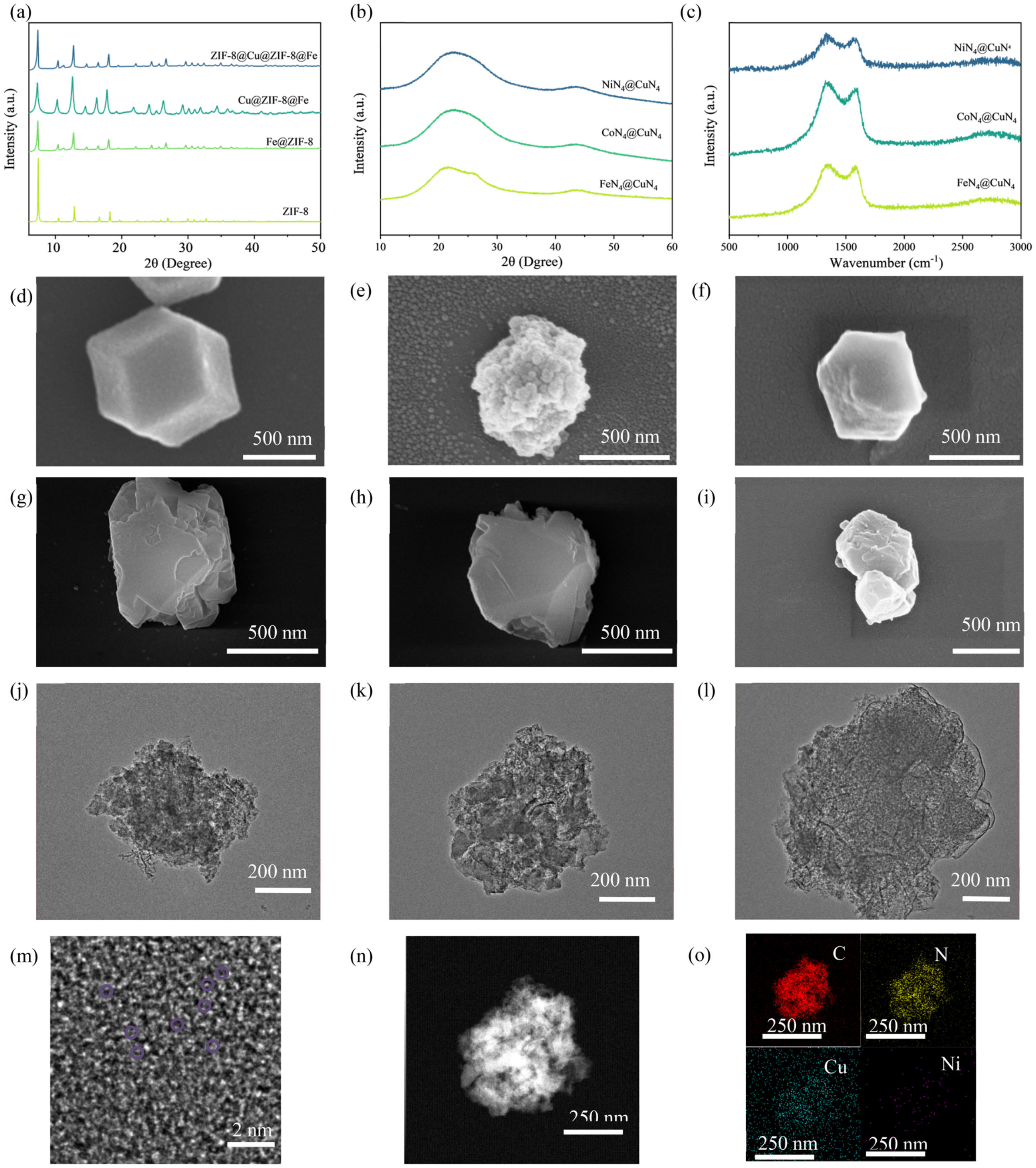

Fig. 2 (a) XRD patterns of ZIF-8, Niphen@ZIF-8, Niphen@ZIF-8@Cuphen and Niphen@ZIF-8@Cuphen@ ZIF-8; (b) XRD patterns of $NiN_4@CuN_4$, $CoN_4@CuN_4$ and $FeN_4@CuN_4$; (c) Raman spectrum of $NiN_4@CuN_4$, $CoN_4@CuN_4$ and $FeN_4@CuN_4$; SEM image of (d) Niphen@ZIF-8, (e) Niphen@ZIF-8@Cuphen, (f) Niphen@ZIF-8@Cuphen@ ZIF-8, (g) $NiN_4@CuN_4$, (h) $FeN_4@CuN_4$ and (i) $CoN_4@CuN_4$; TEM image of (j) $FeN_4@CuN_4$, (k) $NiN_4@CuN_4$ and (l) $CoN_4@CuN_4$; (m) magnified HAADF-STEM image of $NiN_4@CuN_4$; (n) HAADF-STEM image of $NiN_4@CuN_4$; and (o) EDS elemental mappings of C, Cu, N and Ni.

(Fig. 2b) exhibited diffraction peaks consistent with the (002) and (100) planes of graphene, with peak positions of 22.6° and 43.5°, respectively.[33] The Raman spectrum illustrated in Fig. 2c also corroborated the presence of graphene peaks. The sp^2 graphene peaks were observed at 2700 cm^{-1}.[34] This ratio of disorder to graphene peak strength (I_D: I_G) for $NiN_4@CuN_4$ was 1.25, indicating that heat treatment caused obvious defects.[35]

The prepared materials were characterized by SEM (Fig. 2d–i). The Niphen@ZIF-8 sample exhibited a standard ZIF-8 dodecahedral structure with an edge length of approximately 500 nm. The incorporation of Cuphen into Niphen@ZIF-8@Cuphen results in an uneven surface topography. After coating with ZIF-8 and heat treatment again, the $NiN_4@CuN_4$ surface is smooth again and the average crystal width is 550 nm. The successful coating with ZIF-8 is evidenced by the increase in material size and the structural change. The catalysts $CoN_4@CuN_4$ and $FeN_4@CuN_4$ prepared by the same process are shown in Fig. 2e and f. The morphology of the two catalysts is consistent with that of $NiN_4@CuN_4$.

As shown in Fig. 2j–l, $NiN_4@CuN_4$, $CoN_4@CuN_4$ and $FeN_4@CuN_4$ have a clear porous concave dodecahedral structure in the TEM image.

The magnified high-angle annular dark-field scanning TEM (HAADF-STEM) indicates that there are carbon streaks and obvious individual bright spots in the material, with no metallic streaks present, suggesting the successful synthesis of single-atom catalysts (Fig. 2m). $NiN_4@CuN_4$ has a distinct concave dodecahedral structure inside and a concave dodecahedral structure outside, demonstrating the successful synthesis of the double-layered ZIF-8 skeletal structure (Fig. 2n),which is consistent with previous reports.[31] TEM elemental mapping images (Fig. 2o) showed that Ni was uniformly distributed in the innermost layer of $NiN_4@CuN_4$ (inside the inner ZIF-8) and the uniform distribution of Cu was observed in the outer ZIF-8 layer, indicating the successful synthesis of $NiN_4@CuN_4$.

The N_2 adsorption–desorption isotherm is a key indicator of numerous physical characteristics inherent to the tandem catalyst (Fig. 3a). The values of specific surface areas of $NiN_4@CuN_4$, $CoN_4@CuN_4$, and $FeN_4@CuN_4$ were found to be 366.3, 203.7, and 293.5 $m^2\ g^{-1}$, respectively. The elevated specific surface area of $NiN_4@CuN_4$ suggests numerous active sites, consistent with its remarkable catalytic activity. A clear H3 hysteresis loop was observed at medium-pressure ($0.3 < P < 0.8$), without an adsorption plateau at high pressure ($0.8 < P < 1$). The isotherms exhibited characteristics of type IV isotherms. The material displayed clear mesoporous characteristics, with a pore size distribution curve indicating a predominant pore size of 2.3 nm and 8.5 nm (Fig. 3b).

X-ray photoelectron spectroscopy (XPS) analysis of the tandem catalyst provided precise insights into the elemental composition and surface valence states. Fig. S7 depicts the XPS total spectrum of $NiN_4@CuN_4$, which reveals the presence of discernible peaks corresponding to elements such as C, N, Ni, and Cu within $NiN_4@CuN_4$. Limited by the detection depth (~5–10 nm), the photoelectron signals of Cu and Ni are significantly attenuated, especially the Ni 2p orbital cannot be deconvoluted. The contents of Cu and Ni were 1.03 wt% and 2.32 wt% (Table S1), respectively, which were measured by ICP-OES quantitative analysis

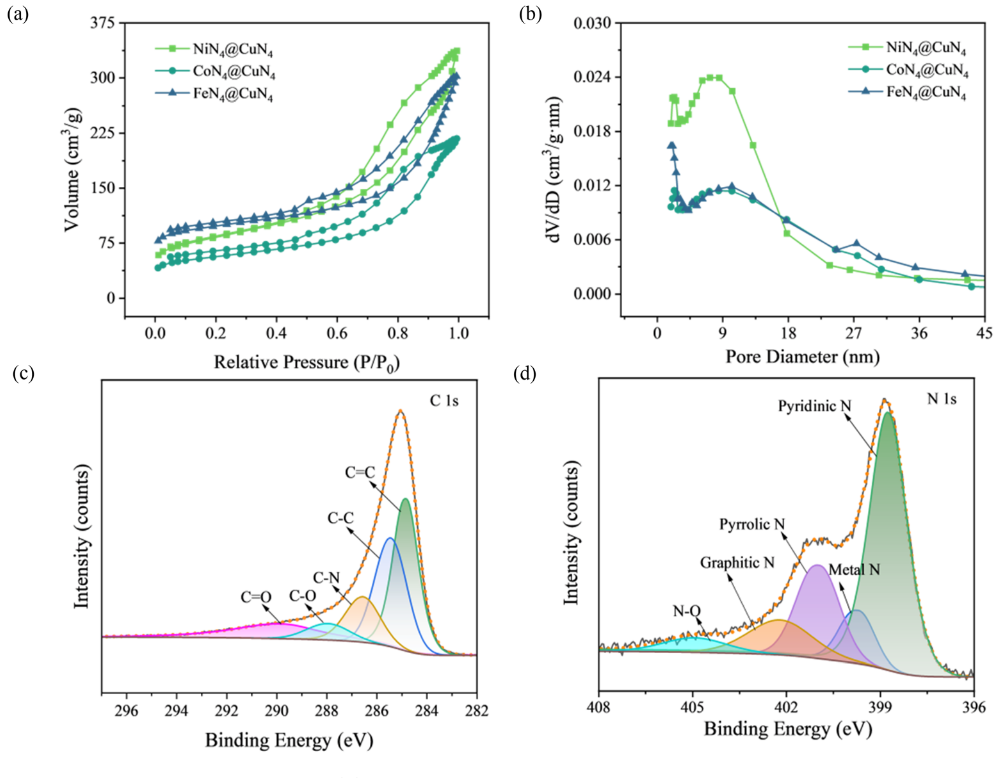

Fig. 3 (a) N_2 adsorption–desorption isotherm curves, (b) pore size distribution of $NiN_4@CuN_4$, $CoN_4@CuN_4$ and $FeN_4@CuN_4$, (c) XPS survey of $NiN_4@CuN_4$, (d) C 1s spectra of $NiN_4@CuN_4$.

(pretreatment of aqua regia digestion). Furthermore, the XPS tests of $CoN_4@CuN_4$ and $FeN_4@CuN_4$ (Fig. S1 and S2) also demonstrated that they contained Fe, Co, N and Cu. The C 1s spectrum of $NiN_4@CuN_4$ is displayed in Fig. 3c. Following deconvolution, the spectrum displays five distinct peaks corresponding to C=C, C–C, C–N, C–O, and C=O bonds.[36] As illustrated in Fig. 3d, the deconvoluted N 1s spectrum is indicative of the presence of pyridinic N (around 398.8 eV), Ni–N and Cu–N (around 399.7 eV), pyrrolic N (around 400.0 eV), graphitic N (around 402.2 eV), and oxidized N (around 404.9 eV). This observation suggests the presence of significant defects in the material and that the metallic elements are anchored by N.[37] This evidence confirms the presence of NiN_4 and CuN_4 species within the catalyst. A combined analysis was undertaken, incorporating scanning electron microscopy, inductively coupled plasma emission spectroscopy, and transmission electron microscopy images. This composite analysis indicated the synthesis of the target product.

3.2 CO_2 electroreduction performance

The CO_2 electroreduction properties of $NiN_4@CuN_4$, $CoN_4@CuN_4$ and $FeN_4@CuN_4$ were investigated using a three-electrode flow cell (Fig. 1c) within 1 M potassium hydroxide solution. Initially, the electrocatalysts were submitted to linear sweep voltammetry (LSV) under a N_2 or CO_2 atmosphere (Fig. S3), where all three catalysts had much higher current densities than the hydrogen evolution reaction (HER). Fig. 4a compares the current densities of the three catalysts under a CO_2 atmosphere, with $NiN_4@CuN_4$ having a higher current density of approximately 120 mA cm^{-2} at −1.5 V *vs.* RHE and $FeN_4@CuN_4$ having a more positive onset potential.

Subsequently, we investigated the CO_2 catalytic performance of the catalysts by performing constant potential tests at −1.3 to −1.7 V *vs.* RHE. The *it* curves are shown in Fig. S4. The identification of the products was achieved through the utilization of gas chromatography and ^1H NMR (Fig. 4b and S5). High electron transfer products $CH_3CH_2CH_2OH$, C_2H_4, CH_3COOH and CH_3CH_2OH were obtained on $NiN_4@CuN_4$ with the highest Faraday efficiency (81.0% at −1.6 V *vs.* RHE) with 24.4% $CH_3CH_2CH_2OH$ and 36.6% CH_3CH_2OH. C_2H_4, CH_3COOH and C_2H_5OH could also be obtained on $CoN_4@CuN_4$, which has a Faraday efficiency of 50.4% for C_{2+} with 20.8% CH_3CH_2OH and 13.7% CH_3COOH. $FeN_4@CuN_4$ is less active for C_{2+} products and the products are mainly C_1, which is consistent with the lower onset voltage. CH_4 and HCOOH are the main products, with 45.8% CH_4 and 30.8% HCOOH. This may be because $FeN_4@CuN_4$ produces less CO, which makes the reaction slower and favorable for C_1 generation. Fig. 4c displays the C_2/C_1 ratio of electrocatalytic products for the three catalysts, indicating that the tandem catalytic action of the inner and outer layers in $NiN_4@CuN_4$ promotes C–C bonding processes, whereas $CoN_4@CuN_4$ and $FeN_4@CuN_4$ exhibit distinct behaviors. The C_2/C_1 ratio for $NiN_4@CuN_4$ increased gradually with voltage, indicating that −1.3 to −1.7 V *vs.* RHE is more favorable for $NiN_4@CuN_4$ to produce C_2. The product ratios of the C_2/C_1 class

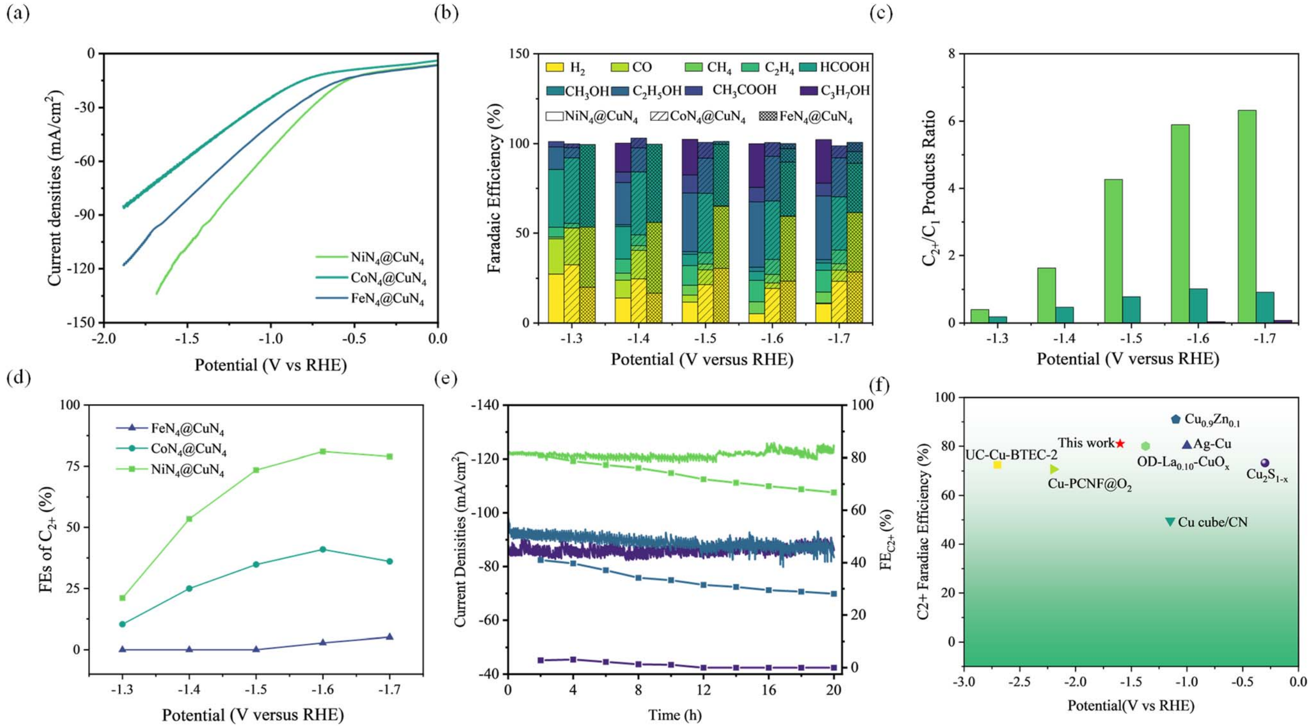

Fig. 4 (a) LSV curves of $NiN_4@CuN_4$, $CoN_4@CuN_4$ and $FeN_4@CuN_4$ in a flow cell, (b) FE of products $NiN_4@CuN_4$, $CoN_4@CuN_4$ and $FeN_4@CuN_4$ in the flow cell, (c) the ratios of FE of C_{2+} and C_1 products on $NiN_4@CuN_4$, $CoN_4@CuN_4$ and $FeN_4@CuN_4$ in the flow cell, (d) FE of C_{2+} products for $NiN_4@CuN_4$, $CoN_4@CuN_4$ and $FeN_4@CuN_4$ in the flow cell at varying positive potentials, (e) stability and $FE_{C_{2+}}$ of $NiN_4@CuN_4$, $CoN_4@CuN_4$ and $FeN_4@CuN_4$ in the CO_2RR at −1.6 V in the flow cell, and (f) comparison of the $FE_{C_{2+}}$ value of $NiN_4@CuN_4$ with other published high-performance Cu-based electrocatalysts.

of products in Fig. 4c demonstrate an enhanced C–C coupling process *via* a yolk–shell structure on NiN_4@CuN_4, in contrast to CoN_4@CuN_4 and FeN_4@CuN_4. This may be attributed to the smaller BET and fewer active sites of CoN_4@CuN_4. The main product of FeN_4@CuN_4 is C_1, and the value of C_2/C_1 is almost 0. The C_{2+} Faraday efficiencies of the three catalysts at different voltages showed a volcano distribution shown in Fig. 4d, in which NiN_4@CuN_4 and CoN_4@CuN_4 reached maxima, 81.0% and 50.4%, respectively, at −1.6 V.

Finally, a long-term electrocatalytic stability test was performed on each of the electrocatalysts at −1.6 V (Fig. 4e). After 20 hours, the current density did not decrease significantly, with NiN_4@CuN_4 exceeding 100 mA cm^{-2}, making it suitable for industrial catalytic applications.

In conclusion, the catalyst NiN_4@CuN_4 exhibited excellent CO_2RR catalytic performance, especially up to 24.4% of $CH_3CH_2CH_2OH$. The catalysts in this work outperformed most reported catalysts (Fig. 4f),[38–44] as shown in Table S1.

3.3 Mechanism analysis

The reaction mechanism of the synthesized electrocatalyst was obtained through electrocatalytic kinetic analysis. As shown in Fig. 5a and S6, cyclic voltammetry was executed on NiN_4@CuN_4, CoN_4@CuN_4, and FeN_4@CuN_4, and their bilayer capacitance values (C_{dl}) were 25.76, 4.73, and 26.73 mF cm^{-2}, indicating higher electrochemical active surface area (ECSA) for NiN_4@CuN_4 and FeN_4@CuN_4. Furthermore, electrochemical impedance spectroscopy (EIS) analysis demonstrated that NiN_4@CuN_4 exhibited superior conductivity as shown in Fig. 5b, thereby potentiating electron transfer at the electrolyte interface. For further exploring generation pathways of CH_3CH_2OH and $CH_3CH_2CH_2OH$, we plotted current density maps (Fig. 5c) and Tafel curves (Fig. 5d) to reveal their kinetic properties. CH_3CH_2OH's part current density on NiN_4@CuN_4 is −35.87 mA cm^{-2} (larger than $CH_3CH_2CH_2OH$'s 23.91 mA cm^{-2}) at −1.6 V, its Tafel slope is 672.94 mV dec^{-1} (smaller than $CH_3CH_2CH_2OH$'s 720.57 mV dec^{-1}), and the data suggest a slower C–C coupling step for $CH_3CH_2CH_2OH$.[45]

To further analyze the CO_2RR mechanism of NiN_4@CuN_4, the evolution of surface intermediates over time (0–40 min) at −1.6 V was investigated employing *in situ* Raman spectra. With the extension of the catalytic time, the characteristic peak of NiN_4@CuN_4 disappears (Fig. 6), and the characteristic band of Cu_2O emerges at 590 cm^{-1}.[46] Subsequent to the restoration of the voltage to the open-circuit voltage, the aforementioned Cu_2O band disappears, thus indicating the consequences of high potentials

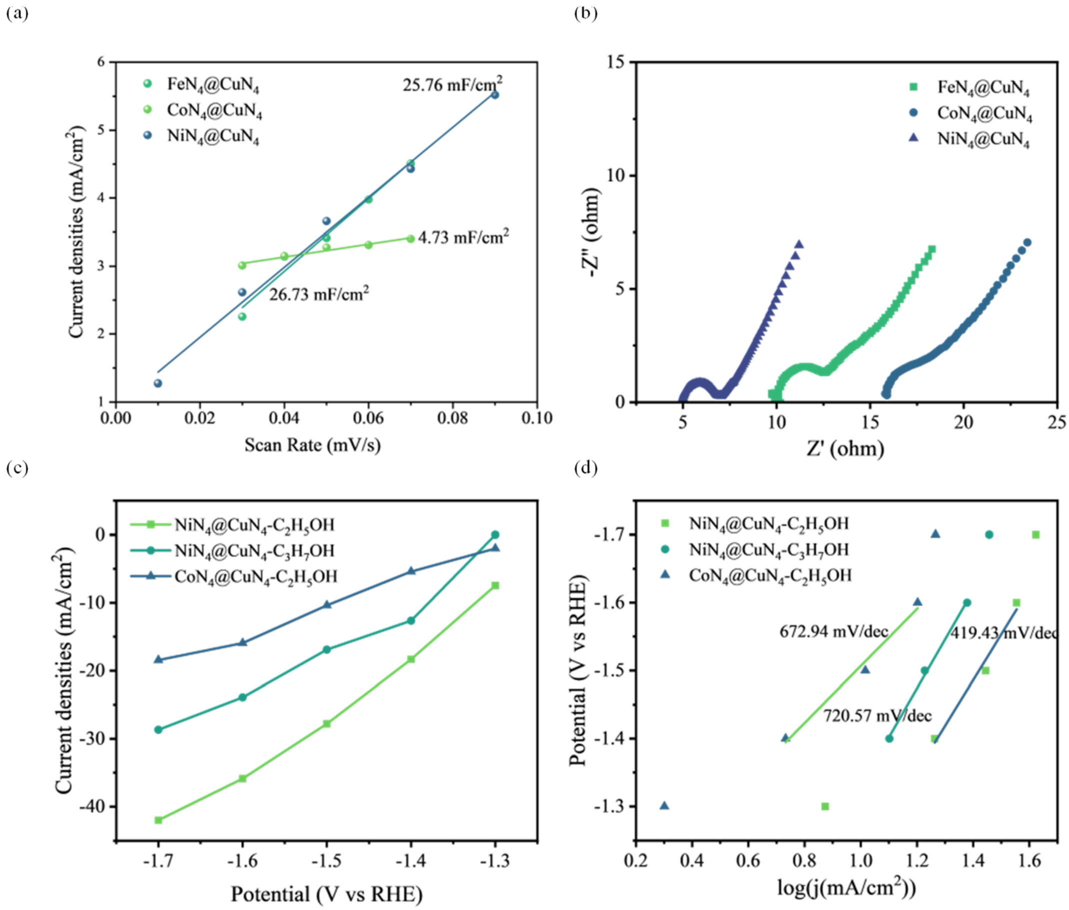

Fig. 5 (a) Electrochemical double-layer capacitance of NiN_4@CuN_4, CoN_4@CuN_4 and FeN_4@CuN_4; (b) electrochemical impedance spectra of NiN_4@CuN_4, CoN_4@CuN_4 and FeN_4@CuN_4; (c) C_2H_5OH and C_3H_7OH part current densities on NiN_4@CuN_4 and CoN_4@CuN_4; and (d) Tafel plots of C_2H_5OH and C_3H_7OH for NiN_4@CuN_4 and CoN_4@CuN_4.

on the catalyst reconfiguration. The –C–OH stretching pattern of the C_2 intermediate (*HOCCOH), observed at 1220 cm^{-1}, provides definitive evidence of C_{2+} generation and validates the easy C–C coupling of $NiN_4@CuN_4$.[47] The peaks observed at 1308 and 1589 cm^{-1} are associated with surface-bound $*CO_2^-$ intermediates,[48] suggesting CO_2 activation *via* $*CO_2^-$ to *CO.

At high potentials, we identified the adsorption bands of *CO (2097–2197 cm^{-1})[49] and found that high *CO coverage is the basis for C–C coupling. Furthermore, C–H signals were observed on the $NiN_4@CuN_4$ surface in the high wave number region, from 2700 to 3200 cm^{-1}.[50] However, due to the complexity of the C–H bonds, reliable conclusions could not be drawn.

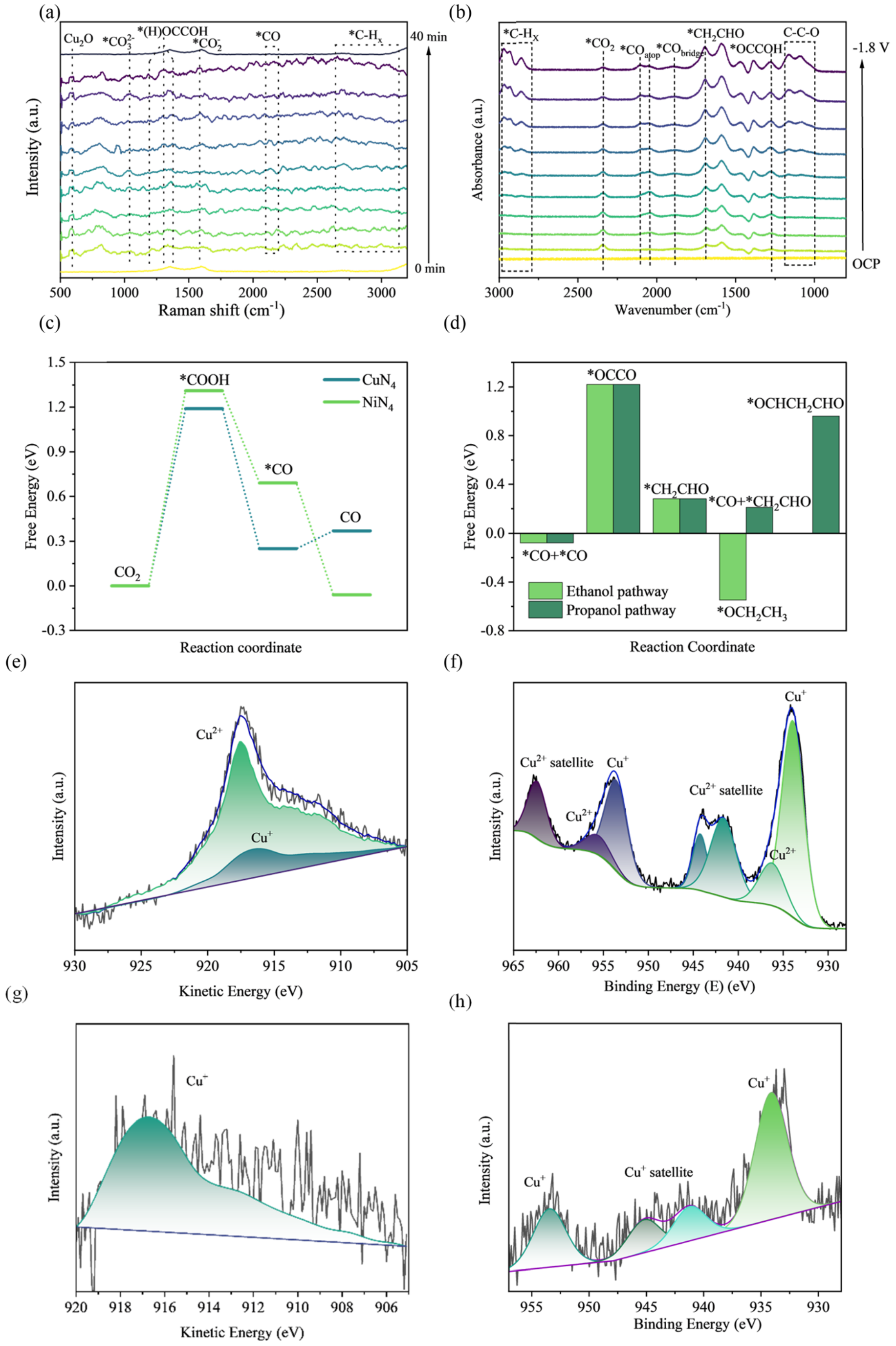

Fig. 6 (a) Carbon dioxide electroreduction at −1.6 V was studied using *in situ* Raman spectroscopy on $NiN_4@CuN_4$ (*in situ* Raman measurements were taken in 0.1 M $KHCO_3$ aqueous solution full of CO_2), (b) carbon dioxide electroreduction from OCP to −1.8 V was studied using *in situ* FTIR spectroscopy on $NiN_4@CuN_4$ (*in situ* FTIR measurements were taken in 1 M $KHCO_3$ aqueous solution full of CO_2), (c) Gibbs free energy diagrams for the hydrogenation of CO_2 to CO on NiN_4 and CuN_4 sites, (d) Gibbs free energy diagrams for the hydrogenation of *CO to $*CH_3CH_2OH$ and $*OCHCH_2CHO$ on CuN_4, (e) Cu Auger spectrum and (f) the Cu 2p spectrum of CuN_4 before catalysis, (g) Cu auger spectrum and (h) Cu 2p spectrum of $NiN_4@CuN_4$ after catalysis.

To investigate the electrocatalytic mechanism of CO_2 conversion on $NiN_4@CuN_4$ further, we performed density functional theory (DFT) calculations (Fig. 6c and d) and *in situ* infrared spectroscopy measurements (Fig. 6b). First, we calculated the pathways for CO_2 hydrogenation to *CO at the NiN_4 and CuN_4 sites. As illustrated in Fig. 6c, the energy barrier for CO_2 conversion to *CO is lower at the CuN_4 site, whereas the barrier for *CO desorption to CO is lower at the NiN_4 site. This suggests that both sites are active for CO_2 activation to CO, but that the CO generated at the NiN_4 site can diffuse to the outer layer and be adsorbed by the CuN_4 site. This result correlates with the continuous depletion of the characteristic peak of gas-phase CO_2 (2346 cm^{-1}) observed *in situ* by infrared spectroscopy. Concurrently, two peaks appear successively at ~2050 cm^{-1} (first) and ~2113 cm^{-1}, which are assigned to CO adsorbed atop the Cu and Ni sites, respectively. Subsequently, a bridged CO signal (~1900 cm^{-1}) emerges and intensifies, creating conditions for C–C coupling.[51]

Secondly, we calculated the pathway at the CuN_4 site, in which *CO and *CO dimerise to form *OCCO. This is then hydrogenated to produce the vital oxygen-containing C_2 intermediate, $*CH_2CHO$. The appearance of a characteristic peak at ~1276 cm^{-1} in the infrared spectrum can be assigned to *OCCOH. Subsequently, the shift of the ~1693 cm^{-1} peak (C=O stretching vibration) clearly indicates the formation of oxygen-containing C_2 intermediates, such as $*CH_2CHO$. Simultaneously, the evolution of the C–H bending vibration (from ~1391 to ~1472 cm^{-1}) was also observed.[52]

Then, DFT calculations were performed to determine the energy barriers for the hydrogenation of CH_2CHO to form CH_3CH_2OH and for $C_1 + C_2$ coupling with CO molecules to form $OCHCH_2CHO$. The results are consistent with previous literature reports and indicate that the energy barrier is $*OCHCH_2CHO > *CH_3CH_2OH$. This aligns with the observed product yields of 28.6% *n*-propanol and 36.6% ethanol. This is attributed to CO overflow from the inner NiN_4 sites forming highly covered *CO on the CuN_4 sites, thereby favoring the formation of *n*-propanol.[53] The electrocatalytic products of the physical mixture of NiN_4 and CuN_4 (NiN_4/CuN_4) (Fig. S8) are solely C_1 and C_2, which further corroborates this. *In situ* infrared fingerprint region data reveal that, following the appearance of the CH_2CHO C=O characteristic peak (at ~1693 cm^{-1}), the double peak in the characteristic fingerprint region representing carbon chain elongation (at ~1161 and 1084 cm^{-1}) appears and intensifies simultaneously, ultimately leading to a significant increase in the intensity of the methyl characteristic peak (at ~2969 cm^{-1}). This provides complete spectral evidence of the transition from the C_2 intermediate to the methyl-containing C_3 product.

In summary, theoretical calculations and *in situ* spectroscopic dynamics corroborate each other, jointly indicating a tandem catalytic pathway. CO_2 is efficiently activated to CO at the inner-layer NiN_4 sites. The CO then diffuses and becomes enriched at the outer-layer CuN_4 sites, forming a bridged adsorption configuration that triggers C–C coupling. This generates an oxygen-containing C_2 intermediate, which then undergoes $C_1 + C_2$ coupling with a second *CO molecule. This enables carbon chain elongation and ultimately hydrogenation, yielding the target product *n*-propanol.

To further investigate the deactivation mechanism of $NiN_4@CuN_4$, we conducted XPS and Cu LMM measurements on $NiN_4@CuN_4$ before catalysis and after 20 h of catalysis. Cu LMM was fitted using the least squares method. As shown in Fig. 6e–h, before catalysis, Cu^{2+} was the predominant species, with an area ratio to Cu^+ of 4.61. A distinct Cu^{2+} satellite peak (962.39 eV) was observed in the Cu 2p spectrum, consistent with the fitting results. After 20 h of catalysis, Cu^{2+} disappeared, and Cu^+ became the predominant species. Simultaneously, no Cu^{2+} satellite peak (962.39 eV) was detected in the Cu 2p spectrum. In summary, after prolonged electrocatalytic operation, a portion of the Cu^{2+} active sites irreversibly reduced to Cu^+ species. This valence change, accompanied by alterations in the local electronic structure and coordination environment of the sites, weakened their adsorption capacity for the key C_1 intermediate (CO).[54] Consequently, C–C coupling significantly decreased, consistent with the sustained decline in faradaic efficiency for the C_{2+} product. Therefore, the irreversible transformation of active sites from highly active Cu^{2+} into less active Cu^+ species is the core reason for the performance decay of $NiN_4@CuN_4$ in electrocatalysis.

4 Conclusions

In summary, a general strategy was developed for synthesizing Janus catalysts ($MN_4@CuN_4$) with double-layered ZIF-8 as the backbone structure and CuN_4-wrapped MN_4. The inner layer of MN_4 facilitates the release of a high concentration of CO, while the outer layer of CuN_4 promotes carbon–carbon coupling in the CO reduction reaction, thereby achieving tandem catalysis at the nanoscale. Furthermore, the integration of physical characterization, electrocatalytic kinetic analysis and DFT calculation facilitated the observation of the dynamic stabilization signal of $*CO_{atop}$, along with the key signal of $*CO_{bridge}$, *OCCOH, during the CO_2RR process. This enabled the efficient synthesis of the C_{2+} product. Among them, the $NiN_4@CuN_4$ catalyst demonstrated exceptional performance in the CO_2RR to C_{2+} products in 1 M KOH, exhibiting an excellent FE of 81.0% for the C_{2+} products at a voltage of −1.6, including a noteworthy FE of 24.4% for $CH_3CH_2CH_2OH$. The findings of this study offer novel insights into the design of innovative catalysts and the optimization of CO_2RR performance, particularly in the synthesis of propanol.

Author contributions

Gege Zhang: methodology, conceptualization, formal analysis, data curation, and writing – original draft. Qianyun Tan: visualization, and writing – review. Xiaoyu Xu: visualization, and writing – review. Faqian Liu: supervision, funding acquisition, project administration, visualization, and writing review.

Conflicts of interest

There are no conflicts to declare.

Data availability

All data supporting this study are included in the article and its supplementary information (SI). Supplementary information: characterization, computational methods, synthetic method of NiN_4/CuN_4, X-ray photoelectron spectroscopy, electrochemical data, metal contents data and comparison with other Cu-based catalysts. See DOI: https://doi.org/10.1039/d5ta10322c.

Acknowledgements

We acknowledge the support from the National Natural Science Foundation of China (52073311) and Guangdong Basic and Applied Basic Research Foundation (2023A1515240024 and 2025A1515012908).

References

1 J. W. Ager and A. A. Lapkin, *Science*, 2018, **360**, 707–708.
2 Y. Y. Birdja, E. Pérez-Gallent, M. C. Figueiredo, A. J. Göttle, F. Calle-Vallejo and M. T. M. Koper, *Nat. Energy*, 2019, **4**, 732–745.
3 X. Chen, S. Jia, J. Zhai, J. Jiao, M. Dong, C. Xue, T. Deng, H. Cheng, Z. Xia, C. Chen, X. Xing, J. Zeng, H. Wu, M. He and B. Han, *Nat. Commun.*, 2024, **15**, 7691.
4 E. W. Lees, B. A. W. Mowbray, F. G. L. Parlane and C. P. Berlinguette, *Nat. Rev. Mater.*, 2021, **7**, 55–64.
5 H. Tian, J.-T. Yang, X. Wang, H. Jiao, Z.-F. Gao, K.-Y. Zhu, Q. He and Z.-L. Wang, *Appl. Catal. B Environ. Energy*, 2025, **375**, 125411.
6 J.-Y. Chen, J.-T. Yang, Y.-S. Han, Y.-Q. Huang, N.-N. Tian, J.-H. Li and Z.-L. Wang, *ACS Catal.*, 2025, **15**, 14882–14894.
7 M. Jouny, W. Luc and F. Jiao, *Ind. Eng. Chem. Res.*, 2018, **57**, 2165–2177.
8 X. Su, Z. Jiang, J. Zhou, H. Liu, D. Zhou, H. Shang, X. Ni, Z. Peng, F. Yang, W. Chen, Z. Qi, D. Wang and Y. Wang, *Nat. Commun.*, 2022, **13**, 1322.
9 W. Liu, P. Zhai, A. Li, B. Wei, K. Si, Y. Wei, X. Wang, G. Zhu, Q. Chen, X. Gu, R. Zhang, W. Zhou and Y. Gong, *Nat. Commun.*, 2022, **13**, 1877.
10 Y. Hori, H. Wakebe, T. Tsukamoto and O. Koga, *Electrochim. Acta*, 1994, **39**, 1833–1839.
11 S. Popović, M. Smiljanić, P. Jovanovič, J. Vavra, R. Buonsanti and N. Hodnik, *Angew. Chem., Int. Ed.*, 2020, **59**, 14736–14746.
12 L. Bian, Y. Bai, J.-Y. Chen, H.-K. Guo, S. Liu, H. Tian, N. Tian and Z.-L. Wang, *ACS Nano*, 2025, **19**, 9304–9316.
13 W. Zheng, X. Yang, Z. Li, B. Yang, Q. Zhang, L. Lei and Y. Hou, *Angew. Chem., Int. Ed.*, 2023, **62**, e202307283.
14 Q. He and T.-T. Li, *Chem.–Eur. J.*, 2025, **31**, e202403297.
15 T. Tang, Z. Wang and J. Guan, *Exploration*, 2023, **3**, 20230011.
16 Z. Zhang, Z. Yang, L. Liu, Y. Wang and S. Kawi, *Adv. Energy Mater.*, 2023, **13**, 2301852.
17 Q. Yang, H. Liu, Y. Lin, D. Su, Y. Tang and L. Chen, *Adv. Mater.*, 2024, **36**, 2310912.
18 X.-F. Yang, A. Wang, B. Qiao, J. Li, J. Liu and T. Zhang, *Acc. Chem. Res.*, 2013, **46**, 1740–1748.
19 P. Song, M. Luo, X. Liu, W. Xing, W. Xu, Z. Jiang and L. Gu, *Adv. Funct. Mater.*, 2017, **27**, 1700802.
20 C. Cao, S. Zhou, S. Zuo, H. Zhang, B. Chen, J. Huang, X.-T. Wu, Q. Xu and Q.-L. Zhu, *Research*, 2023, **6**, 0079.
21 S. Chen, X. Li, C.-W. Kao, T. Luo, K. Chen, J. Fu, C. Ma, H. Li, M. Li, T.-S. Chan and M. Liu, *Angew. Chem., Int. Ed.*, 2022, **61**, e202206233.
22 L. Lin, H. Li, Y. Wang, H. Li, P. Wei, B. Nan, R. Si, G. Wang and X. Bao, *Angew. Chem., Int. Ed.*, 2021, **60**, 26582–26586.
23 K. Li, Y. Kuwahara, K. Chida, T. Yoshii, H. Nishihara and H. Yamashita, *Chem. Eng. J.*, 2024, **488**, 150952.
24 J. Pei, H. Shang, J. Mao, Z. Chen, R. Sui, X. Zhang, D. Zhou, Y. Wang, F. Zhang, W. Zhu, T. Wang, W. Chen and Z. Zhuang, *Nat. Commun.*, 2024, **15**, 416.
25 C. Wang, H. Ren, Z. Wang, Q. Guan, Y. Liu and W. Li, *Appl. Catal. B Environ.*, 2022, **304**, 120958.
26 K. Mou, Z. Chen, X. Zhang, M. Jiao, X. Zhang, X. Ge, W. Zhang and L. Liu, *Small*, 2019, **15**, 1903668.
27 W. Ren, X. Tan, C. Jia, A. Krammer, Q. Sun, J. Qu, S. C. Smith, A. Schueler, X. Hu and C. Zhao, *Angew. Chem., Int. Ed.*, 2022, **61**, e202203335.
28 W. Sun, S. Liu, H. Sun, H. Hu, J. Li, L. Wei, Z. Tian, Q. Chen, J. Su and L. Chen, *Adv. Energy Mater.*, 2025, 2500283.
29 F. Chang, C. M. Vis, M. Bergmeijer, S. C. Howes and P. C. A. Bruijnincx, *ChemSusChem*, 2021, **14**, 5328–5335.
30 T. Zhang, J. C. Bui, Z. Li, A. T. Bell, A. Z. Weber and J. Wu, *Nat. Catal.*, 2022, **5**, 202–211.
31 H. Chen, K. Shen, Y. Tan and Y. Li, *ACS Nano*, 2019, **13**, 7800–7810.
32 J. Huang, X. Xiao, S. Xiong, J. Wan and C. Guo, *J. Alloys Compd.*, 2022, **901**, 163636.
33 R. I. Jibrael and M. K. A. Mohammed, *Optik*, 2016, **127**, 6384–6389.
34 B. Das, R. Kundu and S. Chakravarty, *Mater. Chem. Phys.*, 2022, **290**, 126597.
35 A. Kumar, S. Patil, A. Joshi, V. Bhoraskar, S. Datar and P. Alegaonkar, *Appl. Surf. Sci.*, 2013, **271**, 86–92.
36 A. Guan, Z. Chen, Y. Quan, C. Peng, Z. Wang, T.-K. Sham, C. Yang, Y. Ji, L. Qian, X. Xu and G. Zheng, *ACS Energy Lett.*, 2020, **5**, 1044–1053.
37 J. Ma, L. Huang, K. Chen, J. Wang, X. Kang and X. Cao, *J. Colloid Interface Sci.*, 2023, **652**, 1734–1742.
38 B. A, X. Jin, M. Wang, Y. Wang, W. Chen, Z. Wei, Z. Du, X. Liu, Y. Wang and L. Zhang, *Chem. Eng. J.*, 2024, **500**, 157076.
39 Z. Cai, N. Cao, F. Zhang, X. Lv, K. Wang, Y. He, Y. Shi, H. Bin Wu and P. Xie, *Appl. Catal. B Environ.*, 2023, **325**, 122310.
40 C. Guo, Y. Guo, Y. Shi, X. Lan, Y. Wang, Y. Yu and B. Zhang, *Angew. Chem., Int. Ed.*, 2022, **61**, e202205909.
41 Z. Guo, H. Zhu, Z. Yan, L. Lei, D. Wang, Z. Xi, Y. Lian, J. Yu, K. L. Fow, H. Do, J. D. Hirst, T. Wu and M. Xu, *Appl. Catal. B Environ. Energy*, 2025, **364**, 124839.
42 X. Jiang, Y. Zhao, Y. Kong, J. Sun, S. Feng, Q. Hu, H. Yang and C. He, *Chin. J. Catal.*, 2024, **58**, 216–225.

43 J. Zhang, C. Guo, S. Fang, X. Zhao, L. Li, H. Jiang, Z. Liu, Z. Fan, W. Xu, J. Xiao and M. Zhong, *Nat. Commun.*, 2023, **14**, 1298.

44 N. Zhang and Y. Zhang, *Chem. Eng. J.*, 2024, **499**, 156694.

45 S. Hagos, *Results Chem.*, 2023, **5**, 100952.

46 M. Valvo, J. Thyr and T. Edvinsson, *ChemElectroChem*, 2023, **10**, e202300376.

47 C. Long, X. Liu, K. Wan, Y. Jiang, P. An, C. Yang, G. Wu, W. Wang, J. Guo, L. Li, K. Pang, Q. Li, C. Cui, S. Liu, T. Tan and Z. Tang, *Sci. Adv.*, 2023, **9**, eadi6119.

48 W. Wu, K. Bhattacharyya, K. Gray and E. Weitz, *J. Phys. Chem. C*, 2013, **117**, 20643–20655.

49 X. Kong, J. Zhao, J. Ke, C. Wang, S. Li, R. Si, B. Liu, J. Zeng and Z. Geng, *Nano Lett.*, 2022, **22**, 3801–3808.

50 J. Gao, H. Zhang, X. Guo, J. Luo, S. M. Zakeeruddin, D. Ren and M. Grätzel, *J. Am. Chem. Soc.*, 2019, **141**, 18704–18714.

51 M. Moradzaman and G. Mul, *ACS Catal.*, 2020, **10**, 8049–8057.

52 D. Zhong, Q. Fang, R. Du, Y. Jin, C. Peng, D. Cheng, T. Li, T. Zhao, S. Zhang, Y. Zheng, Q. Zhao, Y. Sun and J. Li, *Angew. Chem., Int. Ed.*, 2025, **64**, e202501773.

53 S. J. Raaijman, M. P. Schellekens, P. J. Corbett and M. T. M. Koper, *Angew. Chem., Int. Ed.*, 2021, **60**, 21732–21736.

54 J. Liu, P. Li, J. Bi, S. Jia, Y. Wang, X. Kang, X. Sun, Q. Zhu and B. Han, *J. Am. Chem. Soc.*, 2023, **145**, 23037–23047.